Ultrasonics Sonochemistry 86 (2022) 106041

Contents lists available at ScienceDirect

Ultrasonics Sonochemistry

journal homepage: www.elsevier.com/locate/ultson

Enhanced photoacoustic imaging in tissue-mimicking phantoms using polydopamine-shelled perfluorocarbon emulsion droplets

Mark Louis P. Vidallon [a], Ekaterina Salimova [b,c], Simon A. Crawford [d], Boon Mian Teo [a], Rico F. Tabor [a,*], Alexis I. Bishop [e,*]

[a] School of Chemistry, Monash University, Clayton, VIC 3800, Australia
[b] Australian Regenerative Medicine Institute, Monash University, Clayton, VIC 3800, Australia
[c] Monash Biomedical Imaging, Monash University, Clayton, VIC 3800, Australia
[d] Ramaciotti Centre for Cryo-Electron Microscopy, Monash University, Clayton, VIC 3800, Australia
[e] School of Physics and Astronomy, Monash University, Clayton, VIC 3800, Australia

ABSTRACT

The current work features process parameters for the ultrasound (25 kHz)-assisted fabrication of polydopamine-shelled perfluorocarbon (PDA/PFC) emulsion droplets with bimodal (modes at 100–600 nm and 1–6 μm) and unimodal (200–600 nm) size distributions. Initial screening of these materials revealed that only PDA/PFC emulsion droplets with bimodal distributions showed photoacoustic signal enhancement due to large size of their optically absorbing PDA shells. Performance of this particular type of emulsion droplets as photoacoustic agents were evaluated in Intralipid®–India ink media, mimicking the optical scattering and absorbance of various tissue types. From these measurements, it was observed that PDA/PFC droplets with bimodal size distributions can enhance the photoacoustic signal of blood-mimicking phantom by up to five folds in various tissue-mimicking phantoms with absorption coefficients from 0.1 to 1.0 cm^{-1}. Furthermore, using the information from enhanced photoacoustic images at 750 nm, the ultimate imaging depth was explored for polydopamine-shelled, perfluorohexane (PDA/PFH) emulsion droplets by photon trajectory simulations in 3D using a Monte Carlo approach. Based on these simulations, maximal tissue imaging depths for PDA/PFH emulsion droplets range from 10 to 40 mm, depending on the tissue type. These results demonstrate for the first time that ultrasonically fabricated PDA/PFC emulsion droplets have great potential as photoacoustic imaging agents that can be complemented with other reported characteristics of PDA/PFC emulsion droplets for extended applications in theranostics and other imaging modalities.

1. Introduction

In the last decade, polydopamine (PDA)-based colloidal materials have been continuously developed and improved to provide innovative solutions to challenges in biomedicine. PDA is a brown to black-coloured polymer made by polymerisation of dopamine that can be obtained either via: oxidative polymerisation under basic pH; oxidant- and ultraviolet (UV)-mediated polymerisation at various pH; or electropolymerisation [1–5]. The resulting products of these processes are typically colloidal particles, but due to the adsorbing and amphiphilic nature of PDA, particle and droplet coatings, as well as surface coatings can also be obtained [4,6–8]. This material by itself and as a surface coating exhibits good biocompatibility and anti-biofouling properties, similar to other bioinspired polymers fabricated from analogous precursors, such as melanin and other melanin-like polymers [7,9–11]. Furthermore, this family of bioinspired polymers exhibits unique optical properties, including a wide absorption range from the UV and visible light region to the near-infrared (NIR) region, tuneable fluorescence properties, and photothermal conversion capacity, which are ideal for biomedical applications [4,12,13].

Perfluorocarbon (PFC) emulsion droplets with a PDA shell or coating are multiresponsive colloidal materials with great potential in biomedicine. These colloids can be fabricated via an ultrasonic dispersion–oxidative polymerisation method [14–16]. Low-boiling point PFC cores can be typically activated to form microbubbles either via acoustic droplet vaporisation or heat application [15–20]. Microbubble production from liquid PFC droplets is advantageous in ultrasound imaging, on-demand drug delivery, and theranostics. Incorporation of the PDA as the emulsion shell confers these colloidal materials with the beneficial optical absorption properties of PDA. PDA and other melanin-like polymers can absorb light to produce heat, which is useful for photothermal and photodynamic therapies [2,7,21–23], optically triggered phase change [22–24], and in photoacoustic imaging [2,25,26]. Due to their strong optical absorption across a wide range in the electromagnetic spectrum, PDA can uniquely enhance photoacoustic signals at long wavelengths (NIR), avoiding spectral overlap with other

---

* Corresponding authors.
E-mail addresses: rico.tabor@monash.edu (R.F. Tabor), alexis.bishop@monash.edu (A.I. Bishop).

https://doi.org/10.1016/j.ultsonch.2022.106041
Received 27 February 2022; Received in revised form 10 May 2022; Accepted 14 May 2022

optically absorbing tissue components. With such exclusive advantage, PDA-based nanoparticles have been widely explored for this application [25,27–31]; however, despite the number of these works on PDA, there are still no reports on the application of ultrasonically fabricated emulsion droplets with PDA coating in photoacoustic imaging.

Herein, we explored for the first time the potential of polydopamine-shelled perfluorocarbon (PDA/PFC) emulsion droplets as photoacoustic signal enhancers using tissue-mimicking phantoms. Using different process parameters, including sonication, PDA/PFC emulsion droplets (with either perfluorohexane (PFC) or perfluoropentane (PFP)) with different size distribution modalities were fabricated. To represent a wide range of tissue types, phantoms were designed mainly based on Intralipid® and India ink, which can mimic optical scattering and absorption of tissues, respectively. This work also highlights the use photon trajectory simulations in 3D using a Monte Carlo approach to determine the maximum imaging depth of PDA/PFC emulsion droplets with bimodal distribution, which has a great potential as screening tool and in predicting the *in vivo* efficiency of colloidal photoacoustic imaging agents.

2. Results and Discussion

2.1. Fabrication of PDA/PFC emulsion droplets

Fabrication of PDA/PFC emulsions with bimodal distributions have been reported previously [14–16]. Ultrasound has two essential roles in this process: (1) dispersion of bulk PFC into small droplets; and (2) initiation of dopamine polymerisation. Probe sonication induces acoustic cavitation, the formation and collapse of small dispersed gas bubbles in the mixture, generating a number of physical effects that break macroscopic PFC droplets into fine droplets: high-speed liquid jets, high local temperatures, pressures, shock waves, turbulence, and extreme physical shearing in the medium [32]. At the same time, acoustic cavitation induced by probe sonication initiates PDA polymerisation via oxidising radical formation [32,33]. The interfaces of dispersed droplets are stabilised both by surface-active Pluronic F-127 molecules and adsorbed dopamine oligomers and PDA nanoparticles. PDA polymerisation is also accelerated by the presence of small amounts of cupric ions [34,35] and oxygen [33], encouraging the formation of a discrete polymer shell from the adsorbed dopamine oligomers and PDA nanoparticles.

To prepare PDA/PFC emulsions with unimodal size distribution, Pluronic F-127 concentration was increased, PFC content was decreased, and sonication time prior to dopamine polymerisation was lengthened. As shown in **Figure S1** (See Electronic Supporting Information), increasing the sonication time from 2 min to 10 min causes the bimodality of the droplet size distribution to disappear, producing droplets with unimodal size distributions. This indicates that longer sonication time plays a key role in allowing ultrasound waves to effectively disperse the bulk PFC into small droplets. The requirement for droplets with unimodal distribution are small pre-emulsion droplets, which are stabilised by Pluronic F-127 molecules during the stages of PDA adsorption and polymerisation, yielding the PDA-shelled droplets without coalescence into larger emulsion droplets. The results obtained are in good agreement with the recent findings of Ferri *et al.* [36] on the formation of lipid-shelled, perfluorocarbon nanodroplets.

Using the original method and modified method (See Experimental section), PDA/PFC droplets with bimodal and unimodal size

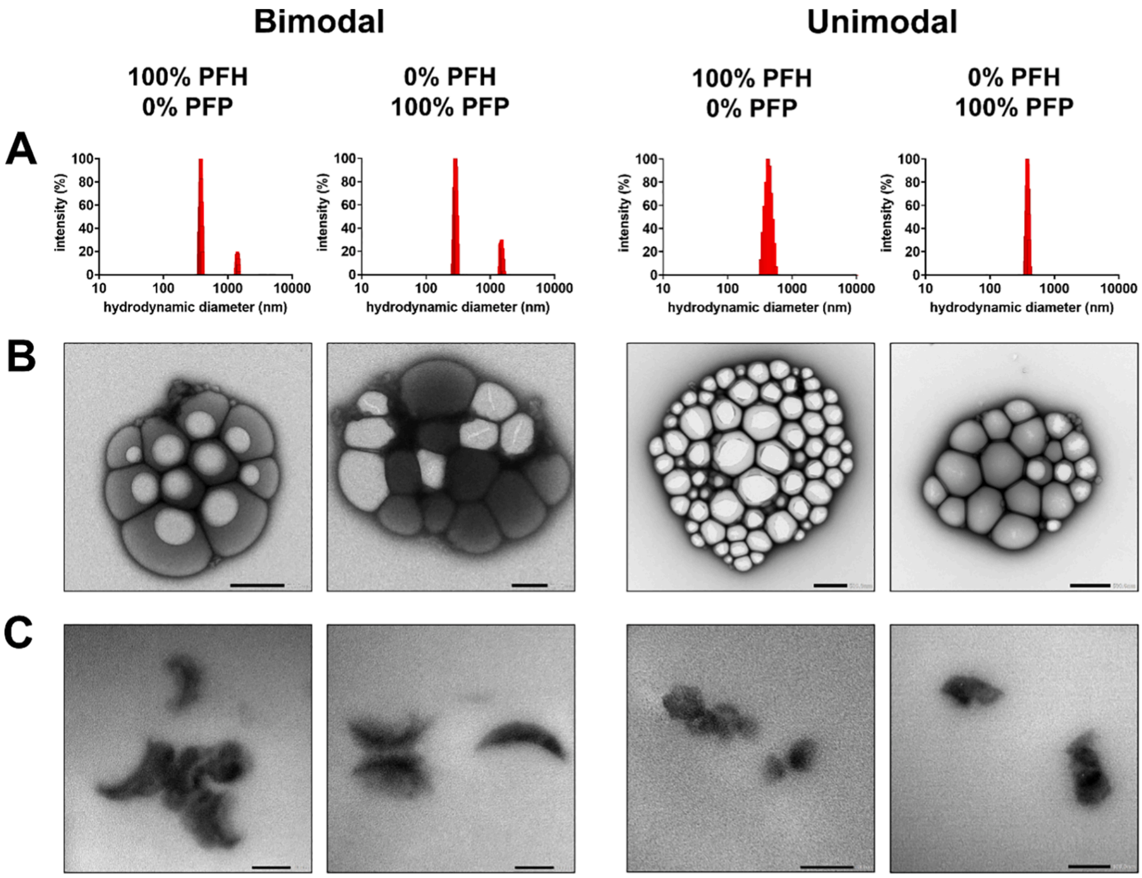

Fig. 1. (**A**) DLS droplet size distributions and (**B** and **C**) transmission electron micrographs of PDA/PFC emulsion droplets with different PFC content and size distribution modality. TEM images in (**B**) show the intact structures of the droplets, while those in (**C**) show ultramicrotomed resin-embedded droplets, revealing the shell or collapsed shell structures. Scale bars = (**B**) 500 nm and (**C**) 100 nm. Photomicrographs of the emulsion droplet samples are shown in Fig. S1 in the Electronic Supplementary Information.

distributions, respectively, were fabricated with different PFCs: perfluorohexane (PFH) and perfluoropentane (PFP). All of the samples had the characteristic black colour of PDA (**Figure S2**, Electronic Supporting Information). Optical microscope imaging (**Figure S3**, Electronic Supporting Information) and dynamic light scattering (DLS) data (Fig. 1**A**) confirmed that the emulsions fabricated using the original method are indeed polydisperse, having bimodal size distributions (modes between 100 and 600 nm and 1–6 μm) and that emulsions fabricated using the modified method have unimodal size distributions (modes between 200 and 600 nm). To visualise submicron-sized droplets, which are difficult to resolve with optical imaging, samples were imaged using transmission electron microscopy (TEM). TEM images, in (Fig. 1**B**), showed droplets with 100 nm–1 μm and 100–600 nm diameters in the bimodal and unimodal samples, respectively, with smooth PDA coating. Droplets with bimodal size distributions appear to be larger and have non-uniform sizes, while droplets with unimodal size distributions are generally smaller with more uniform sizes.

One notable difference between the droplets with bimodal and unimodal size distributions is the shell stability under the electron beam. Droplets with bimodal distributions have higher contrast and are resistant to electron beam damage, unlike the droplets with unimodal distributions that showed shell breakage upon exposure to low dose electron beam. This can be explained by the differences in the shell thicknesses of the droplets with bimodal and unimodal distributions, which was confirmed by imaging resin-embedded droplets that were sectioned into 90-nm thick slices. As shown in (Fig. 1**C**), droplets with bimodal distributions consist of mixtures of micro- and nano-sized PDA shells with a range of morphologies from crescents to hollow circles, which are cross-sections of the original PDA shells with cups and spherical morphologies, respectively, resultant from microtoming the samples. Meanwhile, all samples with unimodal size distributions showed irregularly shaped PDA nanostructures with low contrast, indicative of small PDA quantities and thinness of the shells. This is also supported by the results of phase analysis light scattering (PALS) experiments (**Figure S4**, Electronic Supporting Information), which revealed that the droplets with bimodal size distributions have ζ-potentials around −20 to −30 mV, while those with unimodal size distributions have ζ-potentials around −10 to −20 mV. Observed ζ-potential values indicate differences in the surface charge and suggest a different degree of adsorption of PDA onto the interface of the PFC droplets. These values also indicate that the droplets with bimodal distribution are more colloidally stable, as compared to those with unimodal size distributions. Smaller droplets with unimodal size distributions have larger interfacial areas, in comparison to droplets with bimodal size distributions and larger average diameters, which explains why the former have thinner PDA shells than the latter, given that the same amount of dopamine hydrochloride were used in preparing all the samples.

The observed shell structure difference, however, caused a dramatic difference between the photoacoustic response of the PDA/PFC droplets. As shown in the photoacoustic imaging experiments in water (**Figure S5**, Electronic Supporting Information), the PDA/PFC droplets with unimodal size distribution showed very weak photoacoustic intensity across the wavelength range for photoacoustic imaging. These results indicate that the absorbed amount of radiant energy by the thin PDA shells of the droplets with unimodal distribution from incident light pulses is insufficient to produce detectable acoustic signals within the frequency range of Vevo LZ250 transducer (13–24 MHz). Hence, the only PDA/PFC droplets with bimodal size distributions were used in photoacoustic imaging experiments with tissue-mimicking phantoms.

2.2. *Design of the tissue-mimicking phantoms*

Aqueous dispersions were utilised as tissue-mimicking phantoms, mainly based on two main components: a light scatterer and an absorber. The main property of the light scatterer evaluated for preparing the phantoms is the reduced scattering coefficient (μ_s'). The reduced scattering coefficient of tissues as a function of wavelength can be described using **Equation (1)** with separate contributions of Rayleigh and Mie scattering at the reference wavelength (500 nm).

$$\mu_s'(\lambda) = a'\left(f_{Ray}\left(\frac{\lambda}{500nm}\right)^{-4} + (1 - f_{Ray})\left(\frac{\lambda}{500nm}\right)^{-b_{Mie}}\right) \tag{1}$$

The scaling factor a' equals $\mu_s'(\lambda = 500nm)$. The Rayleigh scattering is $a' \bullet f_{Ray}\left(\frac{\lambda}{500nm}\right)^{-4}$, and the Mie scattering is $a' \bullet \left(1 - f_{Ray}\right)\left(\frac{\lambda}{500nm}\right)^{-b_{Mie}}$, where $1 - f_{Ray}$ indicates the fraction of Mie scattering [37]. Using this equation and the mean values of the parameters for this equation, as summarised by Jacques [37], reduced scattering coefficients of various biological tissues at different wavelengths were calculated. From these calculations, a significant overlap in the reduced scattering coefficient range (10–20 cm^{-1}), shown in **Figure S6** (See Electronic Supporting Information), was observed for almost all tissue types considered (except the skin)—brain, breast, bone, soft tissues, fatty tissues, and fibrous tissues. Hence, the phantom design can be simplified using one type and concentration of the scatterer to represent these multiple tissue types. For this purpose, 1.5 % Intralipid®, which was reported to have a reduced scattering coefficient of 13–15 cm^{-1} [38,39], was used.

India ink was utilised as the other component of the phantoms to simulate optical absorption properties of tissues. Optical absorption coefficients (μ_a) of a dilution series of commercially available India ink were first evaluated as a function of wavelength in the range used in photoacoustic imaging, as shown in Fig. 2**A**. Based on these absorption spectra, relatively low volume concentrations of India ink are needed to mimic the reported absorption properties of various tissues [37,40–42] (**Figure S7**, Electronic Supporting Information). Specifically, to simulate absorption by blood within blood vessels ($\mu_a \approx 4.0$ cm^{-1}), around 0.18 % (v/v) India ink was used in the phantoms and was set as the highest concentration required, as the absorption coefficients of other tissue types are below this value ($\mu_a \approx 0.1$–2.0 cm^{-1}). Instead of designing phantoms for specific tissue types, the phantoms prepared (Fig. 2**B and 2C**) represents a range of tissue types, offering flexibility and adjustability, especially when considering or representing variations in the contents of optically absorbing materials across different tissue and skin types [37,43–45].

2.3. *Photoacoustic imaging of PDA/PFC emulsion droplets in tissue-mimicking phantoms*

Photoacoustic imaging relies on the induction of acoustic radiation by transient temperature changes (photoacoustic effect), caused by a material's absorption of intense pulsed laser radiation [46,47]. Upon irradiation with non-ionising laser pulses, radiant energy is absorbed by the sample and is then converted to head, causing rapid thermoelastic expansion and production of wideband ultrasound emissions that can be detected by a photoacoustic transducer [48,49]. Photoacoustic imaging is a valuable, non-invasive diagnostic imaging modality that offers rich optical contrast and high depth-to-resolution ratio with the aid of endogenous chromophores (haemoglobin, lipids, melanin, *etc.*) and several optically absorbing exogenous colloidal contrast agents (metallic nanoparticles, carbon-based nanomaterials, quantum dots, small organic molecules, semiconducting polymer nanoparticles, *etc.*) [50,51]. Having a broad absorption band ranging from the UV and visible light regions to the near-infrared region and high photothermal conversion efficiency, PDA and other melanin-like materials, such as polymerised catecholamines and biogenic amine neurotransmitters [2,7,9,21–25,28–30,52–55], are ideal photoacoustic imaging/contrast agents, which we explored in this current work.

For the photoacoustic imaging experiments, all samples are dispersed in blood-mimicking phantoms ($\mu_a \approx 4.0$ cm^{-1}) that are confined within polyethylene tubes to simulate the dispersion of PDA/

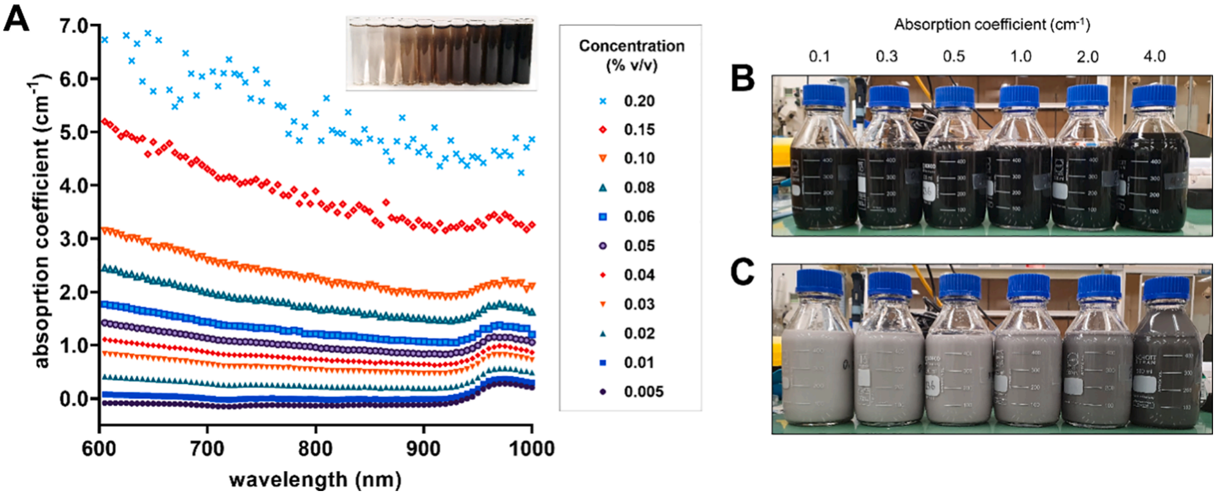

Fig. 2. (**A**) Plot showing the experimental absorption coefficients of India ink at different volume concentrations as a function of wavelength. Inset shows a photograph of aqueous mixtures of India ink at different concentrations. Photographs showing (**B**) aqueous mixtures of India ink at different concentrations (0.017, 0.021, 0.026, 0.034, 0.055, 0.097, and 0.181% (v/v)) and (**C**) the resulting tissue-mimicking phantoms after the addition of Intralipid® dispersion.

PFC droplet in the vasculature. These tubes are fixed onto 3D-printed wells, which were then filled with tissue-mimicking phantoms of lower absorption coefficients ($\mu_a \approx 0.1$–2.0 cm^{-1}) to simulate the tissues surrounding the vasculature (**Figure S8**, Electronic Supporting Information). Fig. 3 shows representative B-mode ultrasound images and corresponding photoacoustic images of the same regions, occupied by blood-mimicking phantoms with different concentrations of PDA/PFH droplets. Based on the images, photoacoustic signal enhancement by the PDA/PFC droplets can only be observed from phantoms with $\mu_a \approx 0.1$ cm^{-1} to 1.0 cm^{-1}. All samples were undetectable in phantoms with higher absorption coefficients. Nevertheless, the effective absorption coefficient range of 0.1–1.0 cm^{-1} is already practically useful for simulating a very wide range of tissue types (**Figure S7**, Electronic Supporting Information); hence, all imaging experiment were conducted using phantoms with this absorption coefficient range.

Images were acquired at 750 nm, 850 nm, and 900 nm, which correspond to photoacoustic intensity peaks of PDA (**Figure S9**, Electronic Supporting Information). Vevo Lab software was used quantify

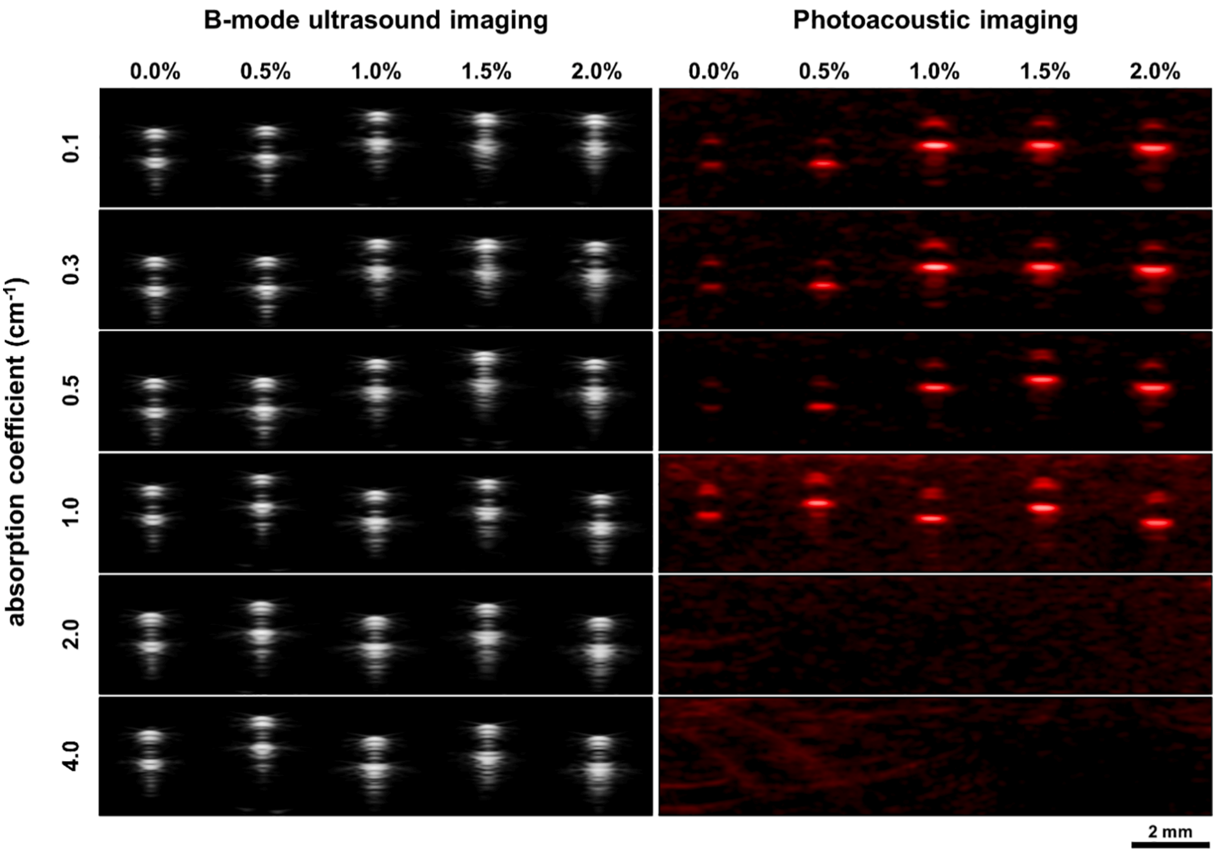

Fig. 3. Representative photoacoustic images of PDA/PFH droplet dispersions at varying concentrations in blood-mimicking phantom ($\mu_a = 4.0$ cm^{-1}) at 750 nm. All tissue-mimicking phantoms have similar Intralipid® concentration ($\mu'_s = 13$–14 cm^{-1}) with different absorption coefficients of 0.1, 0.2, 0.3, 0.5, 1.0, and 2.0 cm^{-1}.

the enhancement of the photoacoustic intensities by the PDA/PFC droplets, which are presented in Fig. 4. Both PDA/PFH and PDA/PFP droplets in the tissue-mimicking phantoms showed generally increasing photoacoustic signal enhancement with increasing concentrations. However, the response between 1.0 and 2.0 % PDA/PFC droplets either plateaus or are not linearly increasing, which is attributable to the either the polydispersity of the sample or the scattering contribution of the larger droplets, especially at higher concentrations. The latter is more evident when the samples are tested in the phantom with the highest absorption coefficient ($\mu_a \approx 1.0\ \mathrm{cm}^{-1}$), wherein maximum signal enhancement was observed with samples of intermediate concentrations. As a positive control, methylene blue, which is a known

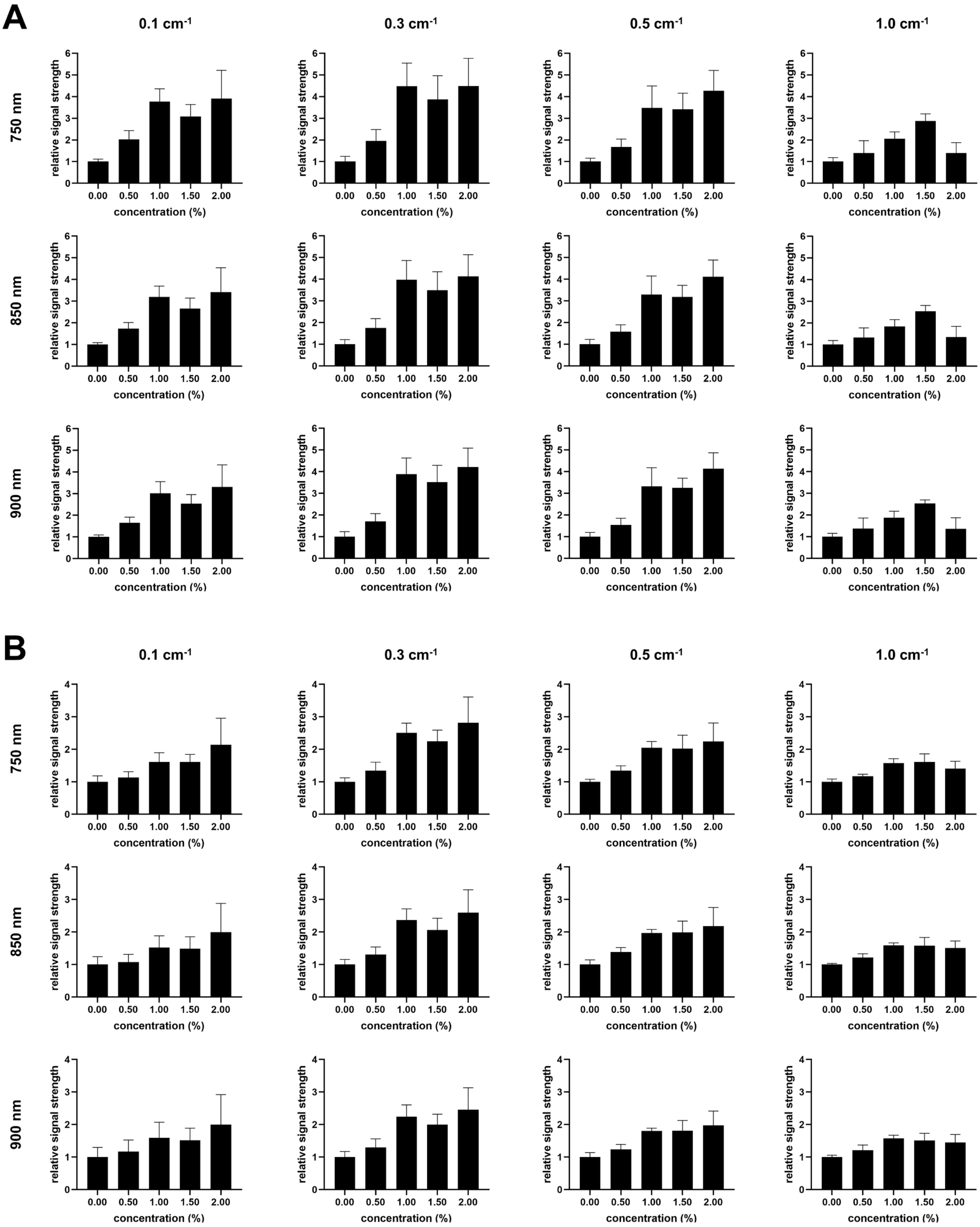

Fig. 4. Plots showing the photoacoustic intensity amplification in different tissue-mimicking phantoms by PDA/PFH and PDA/PFP droplets, relative to the blood-mimicking phantom ($\mu_a = 4.0\ \mathrm{cm}^{-1}$) at different photoacoustic imaging wavelengths. All tissue-mimicking phantoms have similar Intralipid® concentration ($\mu'_s = 13\text{–}14\ \mathrm{cm}^{-1}$) with different absorption coefficients of 0.1, 0.2, 0.3, 0.5, and 1.0 cm^{-1}. Photoacoustic signal enhancement data on their respective PDA shells and on methylene blue (control) are shown in Fig. S10 and S11 in the Electronic Supporting Information.

photoacoustic agent, was used (**Figure S10**, Electronic Supporting Information). PDA/PFC droplets showed evidently higher photoacoustic signal enhancement, despite their lower PDA weight percentages (2.0 % (v/v) PDA/PFC droplets has approximately 0.03 % (w/v) PDA) in comparison to the mass concentration of methylene blue in the test samples. This highlights the advantage of PDA's wide absorption range, which is limited to the visible light range for methylene blue (**Figure S9**, Electronic Supporting Information) and other absorbing molecules and photoacoustic agents.

PDA/PFH droplets had up to two times higher photoacoustic enhancement than PDA/PFP droplets. This can be explained by the differences in the stability of the emulsion droplets. PFP has a boiling point of 28–32 °C while PFH has a boiling point of 58–60 °C. Both boiling points are significantly elevated by decreasing the droplet size due to increased Laplace pressure and the presence of other emulsion components, such as PDA and Pluronic F-127 [16,56–59]. Since the emulsion droplets are polydisperse, despite this stabilising effect, some of the PFP droplets can still become unstable even at room temperature during the preparation and imaging. This results in structural collapse leaving the broken droplet shells, which have lower photoacoustic signal enhancement than the intact emulsion droplets, as shown in **Figure S11** (See Electronic Supporting Information). With the same light intensity for imaging and PDA contents of PDA/PFC droplets and PDA shells in all imaging experiments, it is expected that the energy absorbed per volume in the sample dispersion would be the same for these materials. The most probable contributors to the difference between the droplets and the shells can be deduced from the Grueneisen parameter (**Equation (2)**):

$$G = \propto \nu^{2/C_p} \tag{2}$$

where: $\propto$ is volume expansion parameter; ν is the speed of sound; and C_p is the heat capacity of the material at constant pressure. Since the PDA shell in the PDA/PFC droplets are in intimate contact with the PFC droplet, upon irradiation there will be heat transferred to the internal liquid components, which will contribute to the expansion of the droplet and generation of photoacoustic signal. This generated photoacoustic signal from the emulsion droplets would have a different frequency spectrum as the PDA shells, as the frequency is inversely related to the absorption feature size. Another possible reason for the differences in photoacoustic intensities between the PDA/PFC droplets and the PDA shells is the difference in the frequencies of the photoacoustic signals generated by these two materials, as predicted by the photoacoustic thermoelastic expansion model [60]. Due to their smaller size in comparison with the droplets, PDA shells by themselves would generate photoacoustic spectra with maximum at higher frequency signals, which potentially are undetectable by the photoacoustic imaging system used. PDA/PFC droplets' photoacoustic signals have peak values at lower frequencies, which may have better spectral overlap with the detection range of Vevo LZ250 transducer (13–24 MHz). Photoacoustic imaging parameters that will help improve photoacoustic signals of regions or samples of interest are difficult to adjust (*e.g.* laser intensity), primarily for safety reasons. These results support the idea that varying the structure of colloidal photoacoustic agents is a potential means to enhance their photoacoustic response [61], highlighting that smaller size (submicron) and amount of the colloidal photoacoustic agent exhibits weaker photoacoustic signals [62].

2.4. *Tissue depth limit estimation using PDA/PFH emulsion droplets and the Vevo LAZR photoacoustic imaging system*

The ultimate imaging depth was explored for the PDA/PFH droplets at 750 nm, as these show the greatest enhancement of the PA signal over the blood-mimicking phantom and hence they will provide contrast at the greatest depths. Based on the photoacoustic signal behaviour as a function of absorption coefficient for the phantoms, the minimum fluence was chosen to correspond to 0.25 times the fluence at the sample tubes immersed in the phantom tissue with $\mu_a = 1$ cm^{-1} at 10 mm depth. This is estimated to represent the minimum acceptable signal-to-noise ratio for clear structure recognition. Simulations of the light fluence at these conditions was carried out using the MCmatlab photon transport package [63] implemented in Matlab, which simulates the photon trajectories in 3D using a Monte Carlo approach to determine the expected light fluence as a function of depth for structured light sources. Here, the source was taken as a 24 × 1 mm isotropic radiator to approximately match the output configuration of the Vevo LAZR delivery head. Simulations utilised a simulation volume of between 20 × 20 × 10 mm (x, y, depth) to 20 × 20 × 40 mm depending on the absorption coefficient, and hence penetration depth, with simulation times ranging from 2 to 10 min, depending on the tissue properties. The fluence was evaluated along the scatter-free propagation axis of the beam.

For all simulations, the wavelength is 750 nm, the scattering coefficient $\mu_s = 41.9$ cm^{-1} and the anisotropy parameter $g = 0.656$, which gives a reduced scattering coefficient of $\mu_s' = 14.4$ cm^{-1}. These values represent the scattering properties of 1.5 % Intralipid® (v/v) [38,39,64], and as discussed earlier, are representative of the scattering properties of the majority of mammalian tissue (with the skin as an exception). Simulations used absorption coefficients $\mu_a$ranging from 0.03 to 4 cm^{-1} to cover the reported range of absorption coefficients from mammalian tissue [37,40–42], as shown in **Figure S7** (See Electronic Supporting Information).

A plot of the maximum signal depth as a function of absorption coefficient is shown as Fig. 5. The behaviour is well fitted by a power law curve given by $d_{max} = a.\mu_a{}^b + c$, where $d_{max}$is the maximum imaging depth (mm), μ_a is the absorption coefficient of the tissue (cm^{-1}), $a = 22.47$, $b = -0.2254$ and $c = -10.43$ are fitting parameters. As anticipated, the maximum imaging depth is highly dependent on the absorption coefficient. Imaging depths greater than 10 mm require $\mu_a <$ 1.5 cm^{-1}, which agrees with results shown in Fig. 3, wherein no photoacoustic signal is observable from the tissue phantom with $\mu_a = 2.0$ cm^{-1}.

3. Conclusion

The current work explored for the first time the photoacoustic enhancement capabilities of ultrasonically fabricated PFC emulsion droplets with PDA shells. The role of ultrasound in the fabrication process of PDA/PFC emulsion droplets was highlighted, as well as the effect of other process parameters in controlling the droplet size and polydispersity. Interestingly, it was found that droplet size and distribution modality affect PDA adsorption and hence, the PDA shell thickness. Due to their larger size and thicker PDA coating, only polydisperse droplets with bimodal distribution showed significant photoacoustic signal enhancement at low volume concentrations, while droplets with unimodal size distribution showed no signal enhancement.

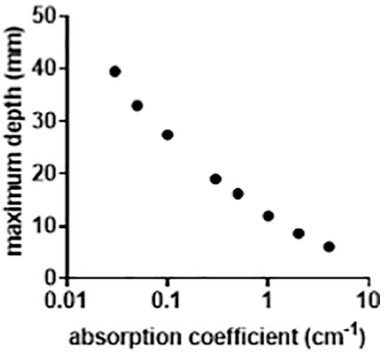

Fig. 5. Plot showing the maximum imaging depth for PDA/PFH droplets at 750 nm, based on 3-D photon trajectory simulations using a Monte Carlo approach.

Performance of PDA/PFC emulsion droplets with bimodal size distributions were evaluated in tissue-mimicking phantoms, which were designed based on Intralipid® and India ink to simulate the optical scattering and absorption properties of tissues, respectively. Results showed that PDA/PFC droplets can significantly enhance photoacoustic imaging of blood vessel phantoms that are submerged in tissue-mimicking phantoms with absorption coefficients from 0.1 to 1.0 cm^{-1}. This absorption coefficient range corresponds to the liver, bladder, brain, breast, heart, and many other tissues, indicating the potential application of these materials *in vivo*. These materials were also shown to enhance photoacoustic signals better than PDA itself and methylene blue (a known photoacoustic agent), which suggest that the photoacoustic properties of PDA are improved when incorporated into colloidal PFC droplets. Photon trajectory simulations in 3D also revealed that maximal tissue imaging depths for PDA/PFH emulsion droplets range from 10 to 40 mm, depending on the tissue type, which correlate well with the photoacoustic imaging data. These findings are important in designing *in vitro* screening methods for photoacoustic agents and prediction of their *in vivo* efficiency, especially with the recent emergence of new generation hybrid materials with potentials beyond photoacoustic imaging.

4. Experimental

4.1. Materials and reagents

Dopamine hydrochloride ($C_8H_{11}NO_7$ HCl, Sigma-Aldrich), copper sulphate, pentahydrate ($CuSO_4 \cdot 5H_2O$, Sigma-Aldrich), Pluronic®F-127 (Sigma-Aldrich), tris(hydroxymethyl)-aminomethane hydrochloride (TRIS HCl, ultrapure, VWR Life Science), perfluoropentane (C_5F_{10}, Synquest Laboratories), perfluorohexane (C_6F_{14}, FluoroChem), and Pebeo Graphic India ink were used as received. Intralipid® (20 %, intravenous injection) was purchased from Team Medical Supplies (NSW, Australia).

4.2. Preparation of PDA/PFC emulsion droplets

The method for the preparation of the PDA/PFC droplets were reported in previous works [14–16]. The 'original' method, which produces polydisperse emulsion droplets with bimodal size distribution, utilised a mixture containing 14.00 mL Tris buffer (10 mol/L, pH 8.5), 5.0 mg Pluronic®F-127, 250.0 μL PFH or PFP, and 130.0 μL $CuSO_4$ solution (40.0 mg mL^{-1}), in a 25 mL glass vial. The vial was submerged in an ice bath and a 3.175 mm diameter ultrasonicator tip (Consonic) was positioned at the half-volume level of the mixture. Immediately before sonication, a freshly prepared mixture of 1.0 mL Tris buffer (10 mol/L, pH 8.5) and 5.0 mg dopamine hydrochloride was added to the suspension. The suspension was then sonicated using a 20 kHz Branson Digital Sonifier SFX 550 (Emerson Electric Co.) for 120 s at 10 % amplitude (power output = 3 W) to yield an emulsion. The vial was removed from the ice bath and then stirred for two hours with the cap/lid off. After stirring, emulsions were divided into 1.50 mL portions, which were then washed twice by centrifugation at 4000 × g for one minute, followed by re-dispersion in 1.00 mL water to remove the unreacted dopamine hydrochloride and excess Tris buffer. The washed, concentrated emulsions were stored at 4 °C until further use.

Monodispersed droplets with unimodal size distributions were prepared in a similar way as described above with higher Pluronic®F-127 mass (75.0 mg) and lower PFH or PFP content (100.0 μL). Furthermore, instead of adding the prepared mixture of 1.0 mL Tris buffer (10 mol/L, pH 8.5) and 5.0 mg dopamine hydrochloride at the start of sonication, the dopamine mixture was added after sonicating the PFC mixture for 8 min, followed by further sonication for 2 min at the same sonication power level. Due to the low photoacoustic signal enhancement of the monodispersed droplets, these materials were not tested in tissue-mimicking phantoms.

4.3. Droplet size analysis and zeta potential measurements

Effective diameters and zeta potentials of the emulsion droplets were determined by DLS and PALS, respectively, using a Brookhaven NanoBrook Omni particle sizer and zeta potential analyser. Samples were also visualised by optical microscopy at 200 × magnification.

4.4. Analysis of PDA shell structure

TEM images were obtained from ultramicrotomed resin slices containing emulsion droplets. Briefly, concentrated emulsions were dispersed in melted 4 % agarose at 40 °C, which was then cooled and transferred into a mixture of Epon resin. The resin, containing the fixed emulsions, was then sectioned into 90 nm slices with a diatome diamond knife using a Leica EM UC7 ultramicrotome (Leica Microsystems). Slices were loaded onto formvar/carbon-coated, 100 mesh copper grids and then imaged using a JEOL JEM-1400Plus TEM (JEOL USA, Inc.) at 80 keV.

4.5. Preparation of tissue-mimicking phantoms

Tissue-mimicking phantoms used as dispersing medium and external phase for imaging were prepared using ultrapure water, India ink, and Intralipid® dispersion. The final concentration Intralipid® in all the phantoms prepared was 1.5 % (v/v) and the concentrations of India ink were 0.017, 0.021, 0.026, 0.034, 0.055, 0.097, and 0.181 % (v/v), corresponding to absorption coefficients of 0.1, 0.2, 0.3, 0.5, 1.0, 2.0, and 4.0 cm^{-1}. Rationalisation of the concentrations of India ink and Intralipid® dispersions used is given in the Results and Discussion.

4.6. Spectrophotometric analysis

All spectrophotometric analyses in this work was performed using a Cary 60 UV–Visible spectrophotometer (Agilent Technologies).

4.7. Photoacoustic imaging

All photoacoustic imaging experiments were performed using Vevo LAZR photoacoustic imaging system (FUJIFILM VisualSonics). Concentrated emulsion samples were dispersed either in water or in blood-mimicking phantom (μ_a = 4.0 cm^{-1}) to obtain final PFC concentrations of 0.0, 0.05, 1.00, 1.50, and 2.00 % (v/v). Methylene blue in either water or blood-mimicking phantom (0.00, 0.05, 0.10, 0.50, 1.00, and 2.00 mg mL^{-1}) was used as a control (molecular photoacoustic agent). Sample dispersions were loaded into polyethylene tubes (0.58 mm and 0.96 mm inner and outer diameters, respectively), which were then fixed into a 3D-printed well (**Figure S8**). The well was placed in a secondary container, filled with either water or the tissue-mimicking phantoms, and then imaged. All photoacoustic images were processed and analysed using Vevo LAB ultrasound analysis software (FUJIFILM VisualSonics).

4.8. Tissue depth limit estimation

The ultimate imaging depth was explored for the PDA/PFH droplets at 750 nm by simulations of the light fluence using the MCmatlab photon transport package [63] implemented in Matlab, which simulates the photon trajectories in 3D using a Monte Carlo approach. Based on the photoacoustic signal behaviour as a function of absorption coefficient for the phantoms, the minimum fluence was chosen to correspond to 0.25 times the fluence at the sample tubes immersed in the phantom tissue with $\mu_a = 1$ cm^{-1} at 10 mm depth. The source was taken as a 24 × 1 mm isotropic radiator, matching the output configuration of Vevo LAZR delivery head. Simulations utilised a simulation voxel volume of 200 × 200 × 200 (x, y, depth), corresponding to a physical volume between 20 × 20 × 10 mm (x, y, depth) to 20 × 20 × 40 mm. Simulation times ranged from 2 to 10 min, depending on the tissue properties. The fluence was evaluated along the scatter-free propagation axis of the beam. For all simulations, the set wavelength is 750 nm, the scattering coefficient $\mu_s = 41.9\ \text{cm}^{-1}$ and the anisotropy parameter $g = 0.656$, and a reduced scattering coefficient of $\mu_s' = 14.4\ \text{cm}^{-1}$. Simulations used absorption coefficients μ_a ranging from 0.03 to 4 cm^{-1}.

CRediT authorship contribution statement

Mark Louis P. Vidallon: Conceptualization, Data curation, Formal analysis, Investigation, Methodology, Writing – original draft, Writing – review & editing. **Ekaterina Salimova:** Investigation. **Simon A. Crawford:** Investigation. **Boon Mian Teo:** Conceptualization, Supervision, Writing – review & editing. **Rico F. Tabor:** Conceptualization, Project administration, Supervision, Writing – review & editing. **Alexis I. Bishop:** Conceptualization, Formal analysis, Methodology, Project administration, Resources, Supervision, Writing – review & editing.

Declaration of Competing Interest

The authors declare that they have no known competing financial interests or personal relationships that could have appeared to influence the work reported in this paper.

Acknowledgement

The authors also acknowledge use of the instruments and scientific and technical assistance at the Monash Centre for Electron Microscopy (MCEM) and Ramaciotti Centre for Cryo-Electron Microscopy, Nodes of Microscopy Australia. The authors also acknowledge the use of equipment and technical assistance at the Monash Biomedical Imaging, during the COVID-19 pandemic. This research is supported by Monash University through the Faculty of Science Dean's Postgraduate Research Scholarships (DPRS and DIPRS), Graduate Research Completion Award (GRCA), and Postgraduate Publication Award (PPA).

Appendix A. Supplementary data

Supplementary data to this article can be found online at https://doi.org/10.1016/j.ultsonch.2022.106041.

References

[1] V. Ball, Polydopamine nanomaterials: recent advances in synthesis methods and applications, Front. Bioeng. Biotechnol. 6 (2018).
[2] J. Park, H. Moon, S. Hong, Recent advances in melanin-like nanomaterials in biomedical applications: a mini review, Biomaterials Research 23 (2019) 24.
[3] K. Jeon, N.M.O. Andoy, C.W. Schmitt, Y. Xue, L. Barner, R.M.A. Sullan, Size-controlled synthesis of bioinspired polyserotonin nanoparticles with free radical scavenging activity, J. Mater. Chem. B 9 (3) (2021) 634–637.
[4] M.E. Lynge, R. van der Westen, A. Postma, B. Städler, Polydopamine—a nature-inspired polymer coating for biomedical science, Nanoscale 3 (12) (2011) 4916, https://doi.org/10.1039/c1nr10969c.
[5] Y.H. Ding, M. Floren, W. Tan, Mussel-inspired polydopamine for bio-surface functionalization, Biosurf. Biotribol. 2 (4) (2016) 121–136.
[6] Z. Lu, L.W. Giles, R.F. Tabor, B.M. Teo, Norepinephrine derived carbon dots for live-cell imaging and effective hemoglobin determination, Soft Matter 17 (28) (2021) 6765–6772.
[7] Z. Lu, A.J. Quek, S.P. Meaney, R.F. Tabor, B. Follink, B.M. Teo, Polynorepinephrine as an efficient antifouling-coating material and its application as a bacterial killing photothermal agent, ACS Appl. Bio. Mater. 3 (9) (2020) 5880–5886.
[8] V. Ozhukil Kollath, M. Derakhshandeh, F.D. Mayer, T. Mudigonda, M.N. Islam, M. Trifkovic, K. Karan, Fluorescent polycatecholamine nanostructures as a versatile probe for multiphase systems, RSC Adv. 8 (56) (2018) 31967–31971.
[9] I. Zmerli, J.-P. Michel, A. Makky, Multifunctional polydopamine-based nanoparticles: synthesis, physico-chemical properties and applications for bimodal photothermal/photodynamic therapy of cancer, Multifunct. Mater. 4 (2) (2021) 022001, https://doi.org/10.1088/2399-7532/abf0fa.
[10] X. Tan, P. Gao, Y. Li, P. Qi, J. Liu, R.u. Shen, L. Wang, N. Huang, K. Xiong, W. Tian, Q. Tu, Poly-dopamine, poly-levodopa, and poly-norepinephrine coatings: Comparison of physico-chemical and biological properties with focus on the application for blood-contacting devices, Bioact. Mater. 6 (1) (2021) 285–296.
[11] Z. Lu, A.M. Douek, A.M. Rozario, R.F. Tabor, J. Kaslin, B. Follink, B.M. Teo, Bioinspired polynorepinephrine nanoparticles as an efficient vehicle for enhanced drug delivery, J. Mater. Chem. B 8 (5) (2020) 961–968.
[12] M. Xiao, M.D. Shawkey, A. Dhinojwala, Bioinspired melanin-based optically active materials, Adv. Opt. Mater. 8 (19) (2020) 2000932.
[13] L. Huang, M. Liu, H. Huang, Y. Wen, X. Zhang, Y. Wei, Recent advances and progress on melanin-like materials and their biomedical applications, Biomacromolecules 19 (6) (2018) 1858–1868.
[14] C. Mannaris, C. Yang, D. Carugo, J. Owen, J.Y. Lee, S. Nwokeoha, A. Seth, B. M. Teo, Acoustically responsive polydopamine nanodroplets: A novel theranostic agent, Ultrason. Sonochem. 60 (2020) 104782, https://doi.org/10.1016/j.ultsonch.2019.104782.
[15] M.L.P. Vidallon, L.W. Giles, S. Crawford, A.I. Bishop, R.F. Tabor, L. de Campo, B. M. Teo, Exploring the transition of polydopamine-shelled perfluorohexane emulsion droplets into microbubbles using small- and ultra-small-angle neutron scattering, PCCP 23 (16) (2021) 9843–9850.
[16] M.L.P. Vidallon, L.W. Giles, M.J. Pottage, C.S.G. Butler, S.A. Crawford, A.I. Bishop, R.F. Tabor, L. de Campo, B.M. Teo, Tracking the heat-triggered phase change of polydopamine-shelled, perfluorocarbon emulsion droplets into microbubbles using neutron scattering, J. Colloid Interface Sci. 607 (2022) 836–847.
[17] Y. Cao, Y. Chen, T. Yu, Y. Guo, F. Liu, Y. Yao, P. Li, D. Wang, Z. Wang, Y.u. Chen, H. Ran, Drug RELEASE FROM PHASE-CHANGEABLE NANODROPLETS TRIGGERED BY LOW-INTENSITY FOCUSED ULTRASOUND, Theranostics 8 (5) (2018) 1327–1339.
[18] D.i. Gao, J. Gao, M. Xu, Z. Cao, L. Zhou, Y. Li, X. Xie, Q. Jiang, W. Wang, J. Liu, Targeted ultrasound-triggered phase transition nanodroplets for Her2-overexpressing breast cancer diagnosis and gene transfection, Mol. Pharm. 14 (4) (2017) 984–998.
[19] S. Mullick Chowdhury, T. Lee, J.K. Willmann, Ultrasound-guided drug delivery in cancer, Ultrasonography 36 (3) (2017) 171–184.
[20] J.Y. Lee, C. Crake, B. Teo, D. Carugo, M. de Saint Victor, A. Seth, E. Stride, Ultrasound-enhanced siRNA delivery using magnetic nanoparticle-loaded chitosan-deoxycholic acid nanodroplets, Adv. Healthcare Mater. 6 (8) (2017) 1601246, https://doi.org/10.1002/adhm.v6.810.1002/adhm.201601246.
[21] Y. Liu, K. Ai, J. Liu, M.o. Deng, Y. He, L. Lu, Dopamine-melanin colloidal nanospheres: an efficient near-infrared photothermal therapeutic agent for in vivo cancer therapy, Adv. Mater. 25 (9) (2013) 1353–1359.
[22] C. Mou, Y. Yang, Y. Bai, P. Yuan, Y. Wang, L. Zhang, Hyaluronic acid and polydopamine functionalized phase change nanoparticles for ultrasound imaging-guided photothermal-chemotherapy, J. Mater. Chem. B 7 (8) (2019) 1246–1257.
[23] J. Zhu, Z. Wang, X. Xu, M. Xu, X.i. Yang, C. Zhang, J. Liu, F. Zhang, X. Shuai, W. Wang, Z. Cao, Polydopamine-encapsulated perfluorocarbon for ultrasound contrast imaging and photothermal therapy, Mol. Pharm. 17 (3) (2020) 817–826.
[24] S. Acter, M.L.P. Vidallon, J.P. King, B.M. Teo, R.F. Tabor, Photothermally responsive Pickering emulsions stabilised by polydopamine nanobowls, J. Mater. Chem. B 9 (43) (2021) 8962–8970.
[25] H. Zhuang, H. Su, X. Bi, Y. Bai, L.u. Chen, D. Ge, W. Shi, Y. Sun, Polydopamine nanocapsule: A theranostic agent for photoacoustic imaging and chemo-photothermal synergistic therapy, ACS Biomater. Sci. Eng. 3 (8) (2017) 1799–1808.
[26] R. Zhong, R. Wang, X. Hou, L. Song, Y. Zhang, Polydopamine-doped virus-like structured nanoparticles for photoacoustic imaging guided synergistic chemo-/photothermal therapy, RSC Adv. 10 (2020) 18016–18024.
[27] L. Zhang, P. Yang, R. Guo, J. Sun, R. Xie, W. Yang, Multifunctional mesoporous polydopamine with hydrophobic paclitaxel for photoacoustic imaging-guided chemo-photothermal synergistic therapy, Int J Nanomedicine 14 (2019) 8647–8663.
[28] H. Hu, Q. Yang, S. Baroni, H. Yang, S. Aime, N.F. Steinmetz, Polydopamine-decorated tobacco mosaic virus for photoacoustic/magnetic resonance bimodal imaging and photothermal cancer therapy, Nanoscale 11 (2019) 9760–9768.
[29] A. Jin, Y. Wang, K. Lin, L. Jiang, Nanoparticles modified by polydopamine: Working as "drug" carriers, Bioact. Mater. 5 (3) (2020) 522–541.
[30] Y. Zhou, B. Lin, K. Li, Y. Zhao, Z. Sun, C. He, R.K. Jha, Preparation of near-infrared/photoacoustic dual-mode imaging and photothermal/chemo synergistic theranostic nanoparticles and their imaging and treating of hepatic carcinoma, Front. Oncol. 11 (2021).
[31] Y. Xie, J. Wang, J. Wang, Z. Hu, A. Hariri, N. Tu, K.A. Krug, M.D. Burkart, N. C. Gianneschi, J.V. Jokerst, J.D. Rinehart, Tuning the ultrasonic and photoacoustic response of polydopamine-stabilized perfluorocarbon contrast agents, J. Mater. Chem. B 7 (31) (2019) 4833–4842.
[32] A. Taha, E. Ahmed, A. Ismaiel, M. Ashokkumar, X. Xu, S. Pan, H. Hu, Ultrasonic emulsification: An overview on the preparation of different emulsifiers-stabilized emulsions, Trends Food Sci. Technol. 105 (2020) 363–377.
[33] H. Mei, Z. Gao, Q. Wang, H. Sun, K. Zhao, P. Zhang, J. Hao, M. Ashokkumar, J. Cui, Ultrasound expands the versatility of polydopamine coatings, Ultrason. Sonochem. 74 (2021) 105571, https://doi.org/10.1016/j.ultsonch.2021.105571.
[34] C. Chen, M. Song, Y. Du, Y. Yu, C. Li, Y.u. Han, F. Yan, Z. Shi, S. Feng, Tumor-associated-macrophage-membrane-coated nanoparticles for improved photodynamic immunotherapy, Nano Lett. 21 (13) (2021) 5522–5531.
[35] M. Salomäki, T. Ouvinen, L. Marttila, H. Kivelä, J. Leiro, E. Mäkilä, J. Lukkari, Polydopamine nanoparticles prepared using redox-active transition metals, J. Phys. Chem. B 123 (11) (2019) 2513–2524.
[36] S. Ferri, Q. Wu, A. De Grazia, A. Polydorou, J.P. May, E. Stride, N.D. Evans, D. Carugo, Tailoring the size of ultrasound responsive lipid-shelled nanodroplets by varying production parameters and environmental conditions, Ultrason. Sonochem. 73 (2021) 105482, https://doi.org/10.1016/j.ultsonch.2021.105482.

[37] S.L. Jacques, Optical properties of biological tissues: a review, Phys. Med. Biol. 58 (11) (2013) R37–R61.

[38] I. Yariv, C. Shapira, H. Duadi, D. Fixler, Media characterization under scattering conditions by nanophotonics iterative multiplane spectroscopy measurements, ACS Omega 4 (10) (2019) 14301–14306.

[39] M. Johns, C.A. Giller, D.C. German, H. Liu, Determination of reduced scattering coefficient of biological tissue from a needle-like probe, Opt. Express 13 (2005) 4828–4842.

[40] A. Hariri, J. Palma-Chavez, K.A. Wear, T.J. Pfefer, J.V. Jokerst, W.C. Vogt, Polyacrylamide hydrogel phantoms for performance evaluation of multispectral photoacoustic imaging systems, Photoacoustics 22 (2021) 100245, https://doi.org/10.1016/j.pacs.2021.100245.

[41] H. Lu, F. Floris, M. Rensing, S. Andersson-Engels, Fluorescence spectroscopy study of protoporphyrin IX in optical tissue simulating liquid phantoms, Materials 13 (9) (2020) 2105, https://doi.org/10.3390/ma13092105.

[42] J.L. Sandell, T.C. Zhu, A review of in-vivo optical properties of human tissues and its impact on PDT, J. Biophotonics 4 (11-12) (2011) 773–787.

[43] D.K. Sardar, M.L. Mayo, R.D. Glickman, Optical characterization of melanin, J. Biomed. Opt. 6 (4) (2001) 404, https://doi.org/10.1117/1.1411978.

[44] C.R. Simpson, M. Kohl, M. Essenpreis, M. Cope, Near-infrared optical properties ofex vivohuman skin and subcutaneous tissues measured using the Monte Carlo inversion technique, Phys. Med. Biol. 43 (9) (1998) 2465–2478.

[45] R.R. Anderson, J.A. Parrish, The optics of human skin, J. Invest. Dermatol. 77 (1) (1981) 13–19.

[46] D. Razansky, 4.19 - Optoacoustic imaging, in: A. Brahme (Ed.), Comprehensive Biomedical Physics, Elsevier, Oxford, 2014, pp. 281–300.

[47] F.M. Mansfeld, T.P. Davis, M. Kavallaris, Chapter two - nanotechnology in medical research, in: M. Skwarczynski, I. Toth (Eds.), Micro and Nanotechnology in Vaccine Development, William Andrew Publishing, 2017, pp. 21–45.

[48] D. Michonneau, P. Bousso, R.S. Negrin, Chapter 4 - in vivo imaging of GVHD and GVL, in: G. Socié, R. Zeiser, B.R. Blazar (Eds.), Immune Biology of Allogeneic Hematopoietic Stem Cell Transplantation (Second Edition), Academic Press, 2019, pp. 51–68.

[49] G.A. Ascoli, J. Bezhanskaya, V. Tsytsarev, Microscopy, in: M.J. Aminoff, R. B. Daroff (Eds.), Encyclopedia of the Neurological Sciences (Second Edition), Academic Press, Oxford, 2014, pp. 16–20.

[50] Q. Fu, R. Zhu, J. Song, H. Yang, X. Chen, Photoacoustic imaging: contrast agents and their biomedical applications, Adv. Mater. 31 (2019), e1805875.

[51] P.K. Upputuri, M. Pramanik, Recent advances in photoacoustic contrast agents for in vivo imaging, WIREs Nanomed. Nanobiotechnol. 12 (4) (2020), https://doi.org/10.1002/wnan.v12.410.1002/wnan.1618.

[52] M. Caldas, A.C. Santos, F. Veiga, R. Rebelo, R.L. Reis, V.M. Correlo, Melanin nanoparticles as a promising tool for biomedical applications – a review, Acta Biomater. 105 (2020) 26–43.

[53] Y. Hu, S. Xue, T. Long, P. Lyu, X. Zhang, J. Chen, S. Chen, C. Liu, X. Chen, Opto-acoustic synergistic irradiation for vaporization of natural melanin-cored nanodroplets at safe energy levels and efficient sono-chemo-photothermal cancer therapy, Theranostics 10 (2020) 10448–10465.

[54] X. Liu, Z. Xie, W. Shi, Z. He, Y. Liu, H. Su, Y. Sun, D. Ge, Polynorepinephrine nanoparticles: A novel photothermal nanoagent for chemo-photothermal cancer therapy, ACS Appl. Mater. Interfaces 11 (2019) 19763–19773.

[55] Y. Xu, W. Li, S. Chen, B. Huang, W. Pei, C. Niu, Near-infrared responsive phase-shifted nanoparticles for magnetically targeted MR/US imaging and photothermal therapy of cancer, Front. Bioeng. Biotechnol. 8 (2020).

[56] N. Rapoport, Phase-shift, stimuli-responsive perfluorocarbon nanodroplets for drug delivery to cancer, WIREs Nanomed. Nanobiotechnol. 4 (5) (2012) 492–510.

[57] P.S. Sheeran, P.A. Dayton, Improving the performance of phase-change perfluorocarbon droplets for medical ultrasonography, Curr. Prog. Challeng. Prosp. Sci. 2014 (2014) 1–24.

[58] N.V. Bulanov, B.M. Gasanov, Peculiarities of boiling of emulsions with a low-boiling disperse phase, Int. J. Heat Mass Transf. 51 (7-8) (2008) 1628–1632.

[59] N.V. Bulanov, B.M. Gasanov, Characteristic features of the boiling of emulsions having a low-boiling dispersed phase, J. Eng. Phys. Thermophys. 79 (6) (2006) 1130–1133.

[60] E.M. Strohm, M.J. Moore, M.C. Kolios, Single cell photoacoustic microscopy: A review, IEEE J. Sel. Top. Quantum Electron. 22 (3) (2016) 137–151.

[61] E.M. Strohm, I. Gorelikov, N. Matsuura, M.C. Kolios, Modeling photoacoustic spectral features of micron-sized particles, Phys. Med. Biol. 59 (2014) 5795–5810.

[62] A.M. Fales, W.C. Vogt, K.A. Wear, I.K. Ilev, T.J. Pfefer, Pulsed laser damage of gold nanorods in turbid media and its impact on multi-spectral photoacoustic imaging, Biomed, Opt. Express 10 (2019) 1919–1934.

[63] D. Marti, R.N. Aasbjerg, P.E. Andersen, A.K. Hansen, MCmatlab: an open-source, user-friendly, MATLAB-integrated three-dimensional Monte Carlo light transport solver with heat diffusion and tissue damage, J. Biomed. Opt. 23 (2018), 121622.

[64] B. Aernouts, R. Van Beers, R. Watté, J. Lammertyn, W. Saeys, Dependent scattering in Intralipid® phantoms in the 600–1850 nm range, Opt. Express 22 (2014) 6086–6098.